Measurement of the Coherent Elastic Neutrino-Nucleus Scattering Cross Section on CsI by COHERENT

D. Akimov,[1] P. An,[2,3] C. Awe,[2,3] P.S. Barbeau,[2,3] B. Becker,[4] V. Belov,[5,1] I. Bernardi,[4] M.A. Blackston,[6] C. Bock,[7] A. Bolozdynya,[1] J. Browning,[8] B. Cabrera-Palmer,[9] D. Chernyak,[7,*] E. Conley,[2] J. Daughhetee,[6] J. Detwiler,[10] K. Ding,[7] M.R. Durand,[10] Y. Efremenko,[4,6] S.R. Elliott,[11] L. Fabris,[6] M. Febbraro,[6] A. Gallo Rosso,[12] A. Galindo-Uribarri,[6,4] M.P. Green,[3,6,8] M.R. Heath,[6] S. Hedges,[2,3] D. Hoang,[13] M. Hughes,[14] T. Johnson,[2,3] A. Khromov,[1] A. Konovalov,[1,5] E. Kozlova,[1,5] A. Kumpan,[1] L. Li,[2,3] J.M. Link,[15] J. Liu,[7] K. Mann,[8] D.M. Markoff,[16,3] J. Mastroberti,[14] P.E. Mueller,[6] J. Newby,[6] D.S. Parno,[13] S.I. Penttila,[6] D. Pershey,[2] R. Rapp,[13] H. Ray,[17] J. Raybern,[2] O. Razuvaeva,[1,5] D. Reyna,[9] G.C. Rich,[3] J. Ross,[16,3] D. Rudik,[1] J. Runge,[2,3] D.J. Salvat,[14] A.M. Salyapongse,[13] K. Scholberg,[2] A. Shakirov,[1] G. Simakov,[1,5] G. Sinev,[2,†] W.M. Snow,[14] V. Sosnovstsev,[1] B. Suh,[14] R. Tayloe,[14] K. Tellez-Giron-Flores,[15] I. Tolstukhin,[14,‡] E. Ujah,[16,3] J. Vanderwerp,[14] R.L. Varner,[6] C.J. Virtue,[12] G. Visser,[14] T. Wongjirad,[18] Y.-R. Yen,[13] J. Yoo,[19] C.-H. Yu,[6] and J. Zettlemoyer[14,§]

[1] *National Research Nuclear University MEPhI (Moscow Engineering Physics Institute), Moscow, 115409, Russian Federation*
[2] *Department of Physics, Duke University, Durham, NC, 27708, USA*
[3] *Triangle Universities Nuclear Laboratory, Durham, NC, 27708, USA*
[4] *Department of Physics and Astronomy, University of Tennessee, Knoxville, TN, 37996, USA*
[5] *Institute for Theoretical and Experimental Physics named by A.I. Alikhanov of National Research Centre "Kurchatov Institute", Moscow, 117218, Russian Federation*
[6] *Oak Ridge National Laboratory, Oak Ridge, TN, 37831, USA*
[7] *Physics Department, University of South Dakota, Vermillion, SD, 57069, USA*
[8] *Department of Physics, North Carolina State University, Raleigh, NC, 27695, USA*
[9] *Sandia National Laboratories, Livermore, CA, 94550, USA*
[10] *Center for Experimental Nuclear Physics and Astrophysics & Department of Physics, University of Washington, Seattle, WA, 98195, USA*
[11] *Los Alamos National Laboratory, Los Alamos, NM, 87545, USA*
[12] *Department of Physics, Laurentian University, Sudbury, Ontario, P3E 2C6, Canada*
[13] *Department of Physics, Carnegie Mellon University, Pittsburgh, PA, 15213, USA*
[14] *Department of Physics, Indiana University, Bloomington, IN, 47405, USA*
[15] *Center for Neutrino Physics, Virginia Tech, Blacksburg, VA, 24061, USA*
[16] *Department of Mathematics and Physics, North Carolina Central University, Durham, NC, 27707, USA*
[17] *Department of Physics, University of Florida, Gainesville, FL, 32611, USA*
[18] *Department of Physics and Astronomy, Tufts University, Medford, MA, 02155, USA*
[19] *Department of Physics and Astronomy, Seoul National University, Seoul, 08826, Korea*

We measured the cross section of coherent elastic neutrino-nucleus scattering (CEvNS) using a CsI[Na] scintillating crystal in a high flux of neutrinos produced at the Spallation Neutron Source (SNS) at Oak Ridge National Laboratory. New data collected before detector decommissioning has more than doubled the dataset since the first observation of CEvNS, achieved with this detector. Systematic uncertainties have also been reduced with an updated quenching model, allowing for improved precision. With these analysis improvements, the COHERENT collaboration determined the cross section to be $(165^{+30}_{-25}) \times 10^{-40}$ cm^2, consistent with the standard model, giving the most precise measurement of CEvNS yet. The timing structure of the neutrino beam has been exploited to compare the CEvNS cross section from scattering of different neutrino flavors. This result places leading constraints on neutrino non-standard interactions while testing lepton flavor universality and measures the weak mixing angle as $\sin^2\theta_W = 0.220^{+0.028}_{-0.026}$ at $Q^2 \approx (50\text{ MeV})^2$.

1. INTRODUCTION

Coherent elastic neutrino-nucleus scattering (CEvNS) is a difficult to measure standard-model

* Now at: Institute for Nuclear Research of NASU, Kyiv, 03028, Ukraine
† Now at: South Dakota School of Mines and Technology, Rapid City, SD, 57701, USA
‡ Now at: Argonne National Laboratory, Argonne, IL, 60439, USA
§ Now at: Fermi National Accelerator Laboratory, Batavia, IL, 60510, USA

process [1, 2], In neutral-current interactions where the momentum transfer (Q^2) is low, the neutrino interacts coherently with the nucleus. The recoil energy transferred to the nucleus is observable, though typical recoil energies are low, tens of keV for neutrino energies in the tens of MeV range. Thus, detectors with low-energy thresholds are required for CEvNS measurement.

CEvNS has the largest cross section among neutrino scattering channels for $E_\nu < 100$ MeV for most target nuclei. For example, inverse beta decay on free protons, the process used for the first detection of the neutrino [3], has a cross section three orders of magnitude lower than CEvNS in CsI. The standard-model prediction depends on the nuclear weak charge, $Q_W^2 = (N-(1-4\sin^2\theta_W)Z)^2 \approx N^2$, where N and Z are the neutron and proton numbers of the target nucleus, and θ_W is the weak mixing angle [4]. Despite the large cross section, 43 years elapsed after the first theoretical prediction of CEvNS before the first experimental observation was realized [5], followed shortly by [6], because of the demanding threshold and background requirements. The challenge was finally overcome using low-threshold detectors in an intense, pulsed source of low-energy neutrinos, such as those produced at the Spallation Neutron Source (SNS) [7, 8] at Oak Ridge National Lab.

The COHERENT experiment deploys a number of detectors designed to measure CEvNS and other low-energy scattering processes, such as $^{40}\mathrm{Ar}(\nu_e, e)$ and neutrino-induced neutron emission, using the π^+ decay-at-rest (πDAR) neutrino flux, attractive for CEvNS measurements [9], produced as a byproduct of SNS operations. The detectors are situated in "Neutrino Alley", a basement hallway where background neutrons from the facility are heavily suppressed and cosmogenic background sources are attenuated with an 8 m.w.e. (meter water equivalent) overburden allowing precision CEvNS measurements. The first experimental demonstration of the existence of CEvNS was made in Neutrino Alley, 19.3 m from the neutrino source using a 14.6 kg CsI[Na] scintillating detector [5]. COHERENT also made the first detection of CEvNS on argon [6], which, together with the initial CsI[Na] measurement, agrees with the N^2 scaling of the cross section predicted by the standard model. While these campaigns were highly successful, they suffer from large statistical and systematic uncertainties, which limit their sensitivity to searches for new physical phenomena.

CEvNS is a precisely predicted neutrino interaction within the standard model. The theoretical uncertainty is primarily dominated by understanding of the spatial distribution of the weak charge in the nucleus. As a result of the clean theoretical predictions, CEvNS is a process well suited for probing physics beyond the standard model (BSM).

A precision measurement of CEvNS is sensitive to the presence of new particles, such as a dark photon that interferes with Z exchange in the low-Q^2 regime [10–12] and may explain the g-2 anomaly [13]. Similarly, through the reliance of Q_W^2 on $\sin^2\theta_W$, CEvNS may identify new physics through an unexpected value of the weak mixing angle at $Q^2 \approx (50\ \mathrm{MeV})^2$ [12]. It can shed light on new forces at high mass scales through non-standard interactions (NSI) searches [14], the understanding of which is very important for interpreting neutrino oscillation measurements, as certain scenarios can obfuscate the interpretation of results [15, 16]. Understanding the CEvNS cross section for different flavors of neutrino is important for disentangling NSI effects from oscillation data making experiments with access to multiple neutrino flavors desirable.

Accelerator-based detectors sensitive to CEvNS are also probes of light, sub-GeV dark matter particles [17, 18] which may be produced at those facilities. Further, CEvNS from solar, atmospheric and diffuse galactic supernova neutrinos are a background for dark matter direct detection experiments [19–21], making up the so-called neutrino floor, so that a clear understanding of their interaction will soon become paramount.

Soon after its prediction, CEvNS was understood to play an important role in energy transport within core-collapse supernova [22–24]. Though uncertainties in the collapse mechanism complicate the role of CEvNS [25], experimental confirmation of the standard-model cross section will help cement these dynamical models. CEvNS will also likely play a role in measuring a future supernova neutrino burst [26, 27]. As a neutral-current process, CEvNS is sensitive to the total neutrino flux, which is of particular interest as other detection channels are most sensitive to the ν_e [28] or $\bar{\nu}_e$ [29] flux.

CEvNS is also a direct test of the weak charge distribution in the nucleus, through the reliance of the cross section on the nuclear form factor [30]. Current data can improve constraints on the charge radius of the neutrino, while future, large CEvNS detectors may measure the parameter [12].

It is with precision measurements of CEvNS that these physics searches are realized. The first such steps are presented here with an updated CsI[Na] dataset and improved understanding of systematic uncertainties. Leveraging the time structure of the neutrino flux from πDAR, leading constraints on non-standard neutrino interactions are presented, along with a direct measurement of the weak mixing angle at low Q^2.

2. EXPERIMENTAL SETUP

We used a 14.6-kg scintillation CsI[Na] crystal [5]. The dopant was selected to reduce the rate of afterglow scintillation following a burst of activity in the detector [31]. The crystal was attached to a single Hamamatsu R877-100 photomultiplier (PMT) for light collection. The signal was digitized at a rate of 500 MS/s with a dynamic range extending beyond our calibration scale, 60 keV$_{ee}$. This crystal was shielded with both low-activity lead and low-Z materials to mitigate γ and neutron backgrounds [31, 32]. Muon veto panels surroundeded the detector which allowed us to remove events with cosmic-associated activity. The detector was placed 19.3 m from the SNS target in Neutrino Alley.

Our dataset includes 13.99 GWhr of integrated beam power that passes livetime criteria on beam stability, detector condition, and afterglow rate described in Sec. 3. During data collection, the SNS ran using a mercury target with a mean beam energy of 0.984 GeV yielding 3.20×10^{23} protons-on-target (POT). Averaged over beam energies, a pion yield of 0.0848 $\pm$ 10% π^+/POT is expected from a GEANT4 [33] simulation of the SNS beam [34]. Data from the SNS on the current through the target was used to extract the timing distribution of POT averaged over the running period. The timing distribution of the POT pulse, averaged over CsI data-taking, has a FWHM of 378 ns. Since this is less than the muon lifetime, the flux separates into two populations: a prompt, predominantly ν_μ flux from π^+ decay followed by a delayed flux of ν_e and $\bar{\nu}_\mu$ from subsequent μ^+ decay. Over 99% of the SNS neutrino flux is generated by π^+ decay-at-rest [34] which has a very well understood time profile.

3. DATA ANALYSIS

Our analysis procedure closely parallels the approach described in [5, 35] with improvements to our simulation, re-optimization of our event selection, and a more thorough detector response model. We performed a two-dimensional log-likelihood fit in recoil energy and time to measure the CEvNS cross section comparing selected data and expected signal and background distributions. Event time and energy were reconstructed by analyzing the PMT waveform in the beam window. We then selected CEvNS candidate events using this reconstruction information.

To generate our predicted signal distribution, we accounted for detector response effects such as quenching, detection efficiency, and energy smearing. Steady-state backgrounds were assessed in-situ with out-of-time beam data and beam-related backgrounds were estimated using data taken previously in Neutrino Alley. Uncertainties in signal and background rates and our detector response were included in the likelihood fit.

3.1. Waveform Reconstruction and Data Selection

The PMT voltage traces were digitized and a 70 μs waveform was saved for every beam spill. The POT signal was set at the 55 μs mark in the waveform. An example waveform is shown in Fig. 1. Following the arrival of the beam, we formed a 15 μs region-of-interest (ROI). The baseline was monitored, and photo-electron (PE) pulses were detected by comparing the digitized PMT voltage to a threshold set above the electronic noise level. Following the first reconstructed photo-electron (PE) pulse in the ROI, we formed a 3 μs integration time to capture most light given by a dominate scintillation decay constant $\tau = 0.6$ μs [31]. We also analyzed a 40 μs pretrace region (PT) immediately preceding the ROI which monitors afterglow activity in the crystal on a spill-by-spill basis. There is an analogous ROI region preceding the POT signal, again with a 40 μs pretrace region. These two ROI regions are called coincidence (C) and anti-coincidence (AC), respectively. As the AC region precedes the beam, we used this timing region to assess beam-uncorrelated backgrounds in-situ while properly sampling detector running conditions.

The detector was calibrated with the 59.5 keV γ decay of an ^{241}Am source. With a Gaussian fit to calibration data, we found a light yield of 13.35 PE/keV. Calibration data were taken with the source at nine different locations along the crystal, finding a spatial spread in light yield less than 3%. This is negligible compared to other identified energy smearing effects. The single PE (SPE) charge was monitored during SNS running by tagging single PMT pulses with little other activity in the crystal.

3.2. Event Selection

Backgrounds producing afterglow contamination in the signal ROI are more likely to have more activity in the pretrace region; we therefore only selected events with five or fewer pretrace pulses. This cut was determined by optimizing our sensitivity to measuring CEvNS given signal and background rates expected for each cut value. We also removed events that have a pulse within the last 200 ns of the pretrace which are typically background events that

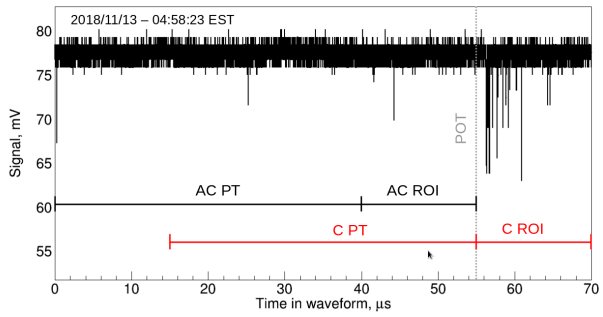

Figure 1. Timing regions of our CsI waveform reconstruction. Events were reconstructed in the 15 μs-long C and AC ROI periods. From the first PE peak in the ROI, we formed a 3 μs integration window. Before each ROI, there is a 40 μs-long pretrace to monitor the instantaneous afterglow rate. The beam arrives at 55 μs, at the beginning of C ROI.

scatter very late in the pretrace and then leak into the ROI. This cut reduced the expected background rate of this type from 40 events to < 1 event in our analysis sample while reducing the signal efficiency by $< 1\%$.

We also required that at least nine pulses were reconstructed in the integration window. According to simulation, this removed all background from coincidence of afterglow pulses within the integration window. These events are predicted to be biased to early scattering times in the ROI, with approximately exponential shape with $\tau \approx 4$ μs. Using this time dependence, we validated this simulation by comparing the rate and time dependence of the afterglow background using AC data and confirm that a negligible afterglow rate, consistent with 0, is expected after the ≥ 9 pulse cut. This cut has a large effect on our selection efficiency and sets the analysis threshold, at an integral ≈ 7 PE.

3.3. Detector Response and Signal Prediction

We applied nuclear recoil quenching by fitting the scintillation response curve, $E_{ee} = f(E_{nr})$, to five datasets collected in CsI[Na] including three taken by COHERENT, described in an upcoming publication, and two described in [36]. The quenching factor, $f(E_{nr})/E_{nr}$ can be used to translate between recoil energy and observed scintillation. The recoil energies in these datasets spanned from 3 to 63 keVee. To account for shape as a function of E_{nr}, we parameterized the scintillation response curve as a fourth degree polynomial, constrained so that $f(0) = 0$. As horizontal error bars detailed in [36] are described as a "spread" rather than an uncertainty, we performed two fits: one with the horizontal errors equal to the quoted spread and one with horizontal errors equal to 0. The former was taken as our scintillation response model. For our central value fit $\chi^2/\text{dof} = 25.6/30$, while $\chi^2/\text{dof} = 47.4/30$ for the alternative fit. We expanded the error band by a factor of 1.58 so that the adjusted $\chi^2/\text{dof} \leq 1$ for both fits.

The selection efficiency for CEvNS recoils depends on recoil energy, PE, and time, t_{rec}, and is given by

$$\varepsilon(\text{PE}, t_{\text{rec}}) = \varepsilon_E(\text{PE}) \times \varepsilon_T(t_{\text{rec}}) \quad (1)$$

where ε_E and ε_T are the energy-dependent and time-dependent efficiencies with no correlation between recoil energy and time. We estimated ε_E using ^{133}Ba calibration data which gave a sample of Compton-scattered electrons. A coincidence with a backing detector was used to mitigate background and ensure only low-energy forward scattering events were used in the calibration. These data, along with the functional fit and error band are shown in Fig. 2. The error band from the fit covers the observed ^{133}Ba data.

There is a 39% chance that there is at least one afterglow pulse in each waveform ROI. Since we reconstructed t_{rec} as the time of the first pulse in the ROI, it is possible for a CEvNS recoil occurring at late t_{rec} to be rejected because it follows a random pulse.

We estimated ε_T with a data-driven simulation. A library of waveforms from AC data was constructed by selecting exactly one waveform for each hour of detector running. A simulated CEvNS waveform, without baseline or noise effects, was then overlaid on a waveform randomly selected from this library. We took ε_T as the ratio of events selected when simulated at $t = t_{\text{rec}}$ compared to $t = 0$. We also expect signal events that follow a random afterglow pulse but within the 3 μs integration window. These events may be selected, but would have biased recoil energy and time. This background was mitigated by requiring the time difference between the first and second pulse in the ROI be within 520 ns. This cut rejected a negligible fraction of events with properly reconstructed t_{rec} but reduced the fraction of biased events sufficiently that the bias does not noticeably affect the measurement.

To validate this simulation we studied the reconstructed t_{rec} for large PE inelastic signals. Due to the large integral of these events, the onset time is unambiguous. We confirmed that the simulation predicts the fraction of events that are lost due to this timing effect.

Our energy resolution is dominated by photon counting. However, the distribution of SPE charge is broad, $\mu/\sigma \approx 0.5$. We thus also Incorporated variations in SPE pulse integral on a pulse-by-pulse ba-

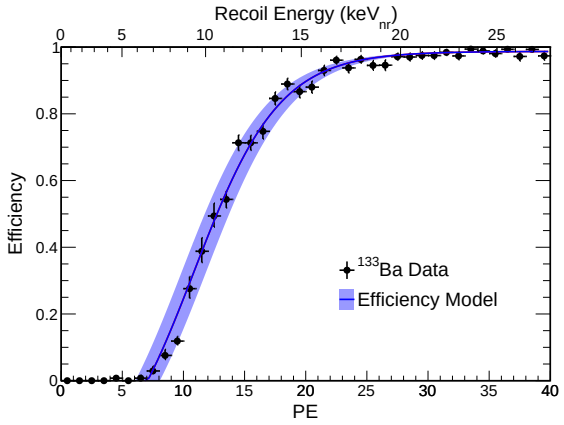

Figure 2. Calibration data using a ^{133}Ba source to estimate our CEvNS selection efficiency along with an error band.

sis into our energy resolution. Combining these two effects, the smearing was modeled with a gamma function

$$P(x) = \frac{(a(1+b))^{1+b}}{\Gamma(1+b)} x^b e^{-a(1+b)x} \qquad (2)$$

which, empirically, fit well to simulated recoil distributions using $a = 1/\text{PE}$ and $b = 0.716 \times \text{PE}$ which appropriately models the asymmetric simulated distribution much better than a Gaussian model.

3.4. Analysis Backgrounds

Over 98% of the analysis background comes from steady-state background that is uncorrelated with the beam. This background is measured in-situ from AC data. We did not observe any correlation between the energy and timing of backgrounds, and so we estimated the PE distribution using all events found in AC data. We used an exponential model for the time distribution with $\tau = 20.2 \pm 2.6$ μs, consistent with the time dependence of the signal efficiency. Uncertainty in this fitted decay constant had a negligible impact on the measured cross section.

We accounted for two sources of beam-related background: beam-related neutron (BRN) and neutrino-induced neutron (NIN) scatters. Prior to detector installation, the normalization of each of these components was studied by an EJ-301 liquid scintillator detector [37] housed in a very similar detector shielding. The neutron-moderating water used in the detector shielding was drained to increase the neutron rate. The BRN and NIN rates were determined from a fit to the time distribution [5]. A MCNPX-PoliMi [38] simulation was used to estimate the total flux of neutrons from each source incident on the EJ-301 detector. This flux was then propagated through the full shielding into the CsI[Na] detector to simulate the neutron background in the detector. We assume a power-law BRN flux, $\phi \propto E^{-\alpha}$, which is consistent with α values between 0 and 2. Changes in the value of α have a negligible effect on the shape of our background distributions. The NIN spectrum was estimated using MARLEY [39, 40] tuned to production on ^{208}Pb with an incident πDAR spectrum, ignoring the decay-in-flight flux as only a handful of NIN events are expected. After applying quenching, energy smearing, and efficiency, we estimated 18 ± 5 (25%) BRN and 6 ± 2 (35%) NIN events in our sample with uncertainty dominated by the statistical precision of the EJ-301 fit [5]. Together BRN and NIN backgrounds are small, about 7% of the predicted CEvNS rate.

It has been suggested that there should be a significant rate of incoherent NC interactions [41] that produce similar nuclear recoils to CEvNS. However, we did not account for this additional production of neutrino-induced recoils.

3.5. Likelihood Fit and Systematic Uncertainties

As we have implemented several improvements to our simulation, selection, and efficiency, the analysis development was blinded. All data in the C region of the ROI were not studied until predictions and uncertainties had been finalized. To validate our updated model for steady-state background events, we first studied a sideband of events with $t_{\text{rec}} > 6$ μs.

We performed a binned likelihood fit to data in both PE and t_{rec}. All data events with PE < 60 and $t_{\text{rec}} < 6$ μs were included in the fit. A non-uniform binning was determined to optimize the statistical power of the fit while maintaining sensitivity to potential systematic effects in the analysis sample. We accounted for correlations between PE and t_{rec} when constructing the CEvNS prediction. All systematic uncertainties wee included as nuisance parameters and appropriately pull on the predicted shape. Uncertainty parameters were profiled in the fit.

We accounted for normalization uncertainty on each component. The CEvNS uncertainty is 10%, dominated by our understanding of the total neutrino flux [34]. We also included a 2.1% uncertainty on the steady-state background normalization due to a finite sample used to estimate the background. The BRN and NIN components have a 25% and 35% uncertainty as described in Sec. 3.4.

We also fit five systematic parameters that affect the shape of our predicted spectra. The timing onset of the neutrino flux through our detector was al-

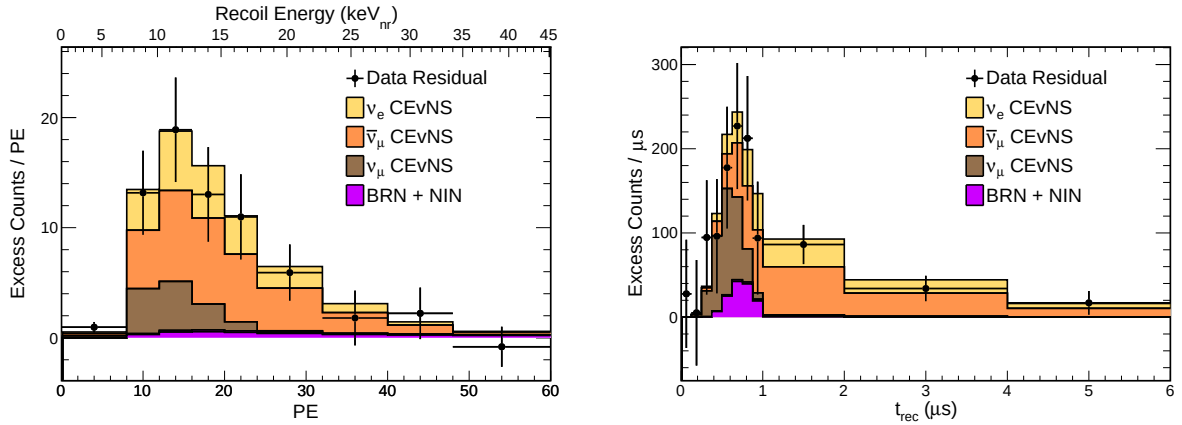

Figure 3. The data residual over steady-state background compared to best-fit CEvNS, BRN, and NIN predictions projected onto the PE (left) and $t_{\rm rec}$ (right) axes. The CEvNS distribution has been decomposed into each flavor of neutrino flux at the SNS.

lowed to float without any prior constraint. We also accounted for uncertainty in the quenching model by performing a principle component analysis (PCA) of the covariance matrix from fit to available data. We identified four uncorrelated quenching shape uncertainties from the PCA, but found only two impact our fit. These two gave a combined 3.8% bias in our fit. A PCA was also performed on our CEvNS efficiency curve from ^{133}Ba calibration data. About 99.9% of the variance is carried by just one systematic parameter which is roughly equivalent to adjusting the threshold by 1.0 PE and gives a 4.1% uncertainty. Finally, our form factor uncertainty adjusts neutron radius in CsI, R_n, by ±5%, which shifts the theoretical CEvNS cross section by 3.4% and gives a 0.6% uncertainty on our measured cross section.

4. RESULTS

After fitting, we observed 306 ± 20 CEvNS events, consistent with the standard-model prediction of 341 ± 11(theory) ± 42(expt.) when accounting for theoretical uncertainty on the form factor and experimental uncertainty on the production and detection of CEvNS. A summary of prior prediction and best-fit event counts is shown in Table I. The best-fit residual CEvNS spectra are shown in Fig. 3 after projecting onto the PE and $t_{\rm rec}$ axes. The best-fit prediction models the observed data well with a $\chi^2/\text{dof} = 82.6/98$. We checked that there is no excess observed in beam-off data to validate analysis software.

The cross section averaged over the $\nu_\mu/\nu_e/\bar{\nu}_\mu$ flux, $\langle\sigma\rangle_\Phi$, was determined by the $\Delta\chi^2$ curve, Fig. 4, after profiling nuisance parameters. Our experimentally-determined CEvNS cross section is $(165^{+30}_{-25}) \times 10^{-40}$ cm^2 which is consistent with the standard-model prediction of $(189 \pm 6) \times 10^{-40}$ cm^2. We tested the validity of Wilks' theorem [42] for this result with a pseudo-experiment coverage test. The observed data reject the no-CEvNS hypothesis at 11.6 σ.

	Prior Prediction	Best-Fit Total
Steady-state background	1286 ± 27	1273 ± 24
BRN	18.4 ± 4.6	17.3 ± 4.5
NIN	5.6 ± 2.0	5.5 ± 2.0
CEvNS	–	306 ± 20

Table I. A summary of prior prediction and best-fit event rates and statistical uncertainties for CEvNS and each background type. The standard-model expectation for CEvNS is $341 \pm 11 \pm 42$.

Since the standard-model cross section depends on the weak charge, the CEvNS cross section can be interpreted as a constraint on the weak mixing angle at a low momentum exchange, $Q^2 \approx (50\ \text{MeV})^2$ similar to previous results [43]. Our current result implies $\sin^2\theta_W = 0.220^{+0.028}_{-0.026}$ compared to the standard-model prediction 0.23857(5) at this Q^2 [44]. Current constraints at low-Q^2 from atomic parity violation measurements are much more precise, though a percent-level measurement will be possible with precision CEvNS detectors in the future. However, as ^{133}Cs is a commonly used atom for these studies [45, 46], CEvNS data can be used to constrain theoretical uncertainties on nuclear structure assumed in these results [4].

Exploiting the differences in timing shapes between the CEvNS contributions from $\nu_\mu, \bar{\nu}_\mu$ and ν_e, we also measured the "flavored" CEvNS cross sections, $\langle\sigma\rangle_\mu$ and $\langle\sigma\rangle_e$, treating each as a completely independent quantity. We do, however, require $\langle\sigma\rangle_\mu$ and $\langle\sigma\rangle_{\bar{\mu}}$ scale the same way relative to their standard-model predictions. This param-

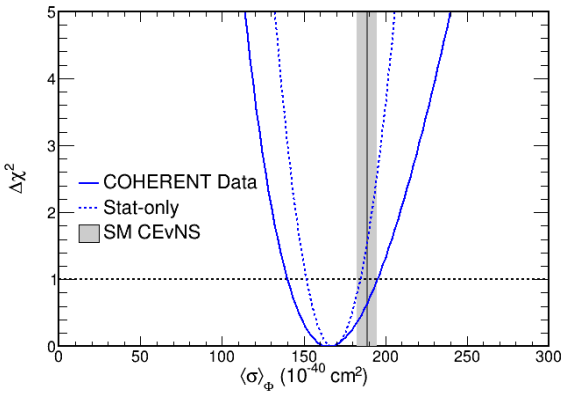

Figure 4. The $\Delta\chi^2$ curve for the CEvNS cross section determined from the fit to data both with and without systematic effects. The standard-model prediction, along with the 1 σ error band from the form factor uncertainty is given by the vertical grey band.

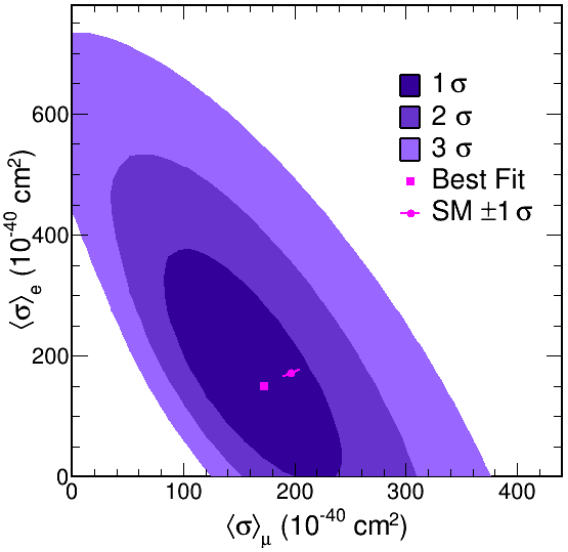

Figure 5. Contours for the flavored CEvNS cross section. The best-fit parameters and the standard-model prediction, along with ± 1 σ error bands from form-factor uncertainty, are shown as pink markers.

eter space is a sensitive probe of BSM physics such as neutrino-quark vector NSI which can affect each neutrino flavor differently [14]. The flavored CEvNS cross section result is uniquely possible using a flux from a spallation sources with beam width less than the muon half-life where flux of ν_μ is separable from the ν_e flux in time.

The allowed contour in this parameter space is shown in Fig. 5. This is consistent with the standard-model cross sections, $\langle\sigma\rangle_\mu = 197 \times 10^{-40}$ cm^2 and $\langle\sigma\rangle_e = 172 \times 10^{-40}$ cm^2, which are somewhat different values due to differences in the energy shape of the neutrino flux for each flavor. The best-fit scales relative to the standard model are 0.876 and 0.873 for $\langle\sigma\rangle_\mu$ and $\langle\sigma\rangle_e$, respectively. Though the total significance of observing CEvNS is very high, $\langle\sigma\rangle_\mu$ and $\langle\sigma\rangle_e$ are found to be non-zero only at 3.0 σ and 1.4 σ, respectively. This is much lower than the total significance of observing CEvNS because both cross sections are allowed to float – a high $\langle\sigma\rangle_e$ can partially compensate for a low $\langle\sigma\rangle_\mu$ and vice versa.

We used this measurement to constrain heavy-mediator, $m_V \gg Q$, neutrino-quark NSI, commonly parameterized as a matrix of ε^f_{ij} where $i, j = e, \mu, \tau$ and $f = u, d$, valid when Q^2 is small compared to the mediator mass. Existence of NSI could confuse ongoing efforts to measure the neutrino mixing matrix parameters. Notably, it is possible to reverse the inferred neutrino mass ordering from oscillation data by choosing a suitable set of NSI parameters [15]. Also, NSI allow for additional CP-violating phases which may bias constraints on δ_{CP} [16].

In Fig. 6, we show the constraint on ε^u_{ee} and ε^d_{ee} with all other parameters fixed to 0 compared to CHARM [47] constraints. This marks a significant improvement over the previous COHERENT constraint from CEvNS on CsI[Na] [5] because of an improved precision result and measuring the flavored cross sections. There are also NSI constraints determined from CEvNS data on Ar [6] and Xe [48], though these limits are currently less precise and not included here.

Fig. 6 also shows our sensitivity to ε^u_{ee} and $\varepsilon^u_{\mu\mu}$. As before, all other NSI parameters are fixed at 0. This combination is directly related to solar neutrino oscillation results. In the context of NSI, there is a degeneracy in oscillation data between the large mixing angle (LMA) and LMA-Dark solutions which differ in the θ_{12} octant and altering the interpretation of the neutrino mass ordering [49]. The shape of the allowed parameter space again highlights the power of the flavored CEvNS measurement as $\varepsilon^{u,V}_{ee}$ and $\varepsilon^{u,V}_{\mu\mu}$ only affect the CEvNS cross section for ν_e- and ν_μ-flavor neutrinos, respectively. If only the total CEvNS cross section were considered, allowed contours would form rings

5. CONCLUSION

We measured the CEvNS cross section using the full dataset collected by the CsI[Na] scintillation detector using a blinded analysis approach. With doubled exposure and improved understanding of systematic uncertainties, we have made the most precise measurement of CEvNS to date, observing CEvNS at 11.6 σ and finding a flux-averaged cross

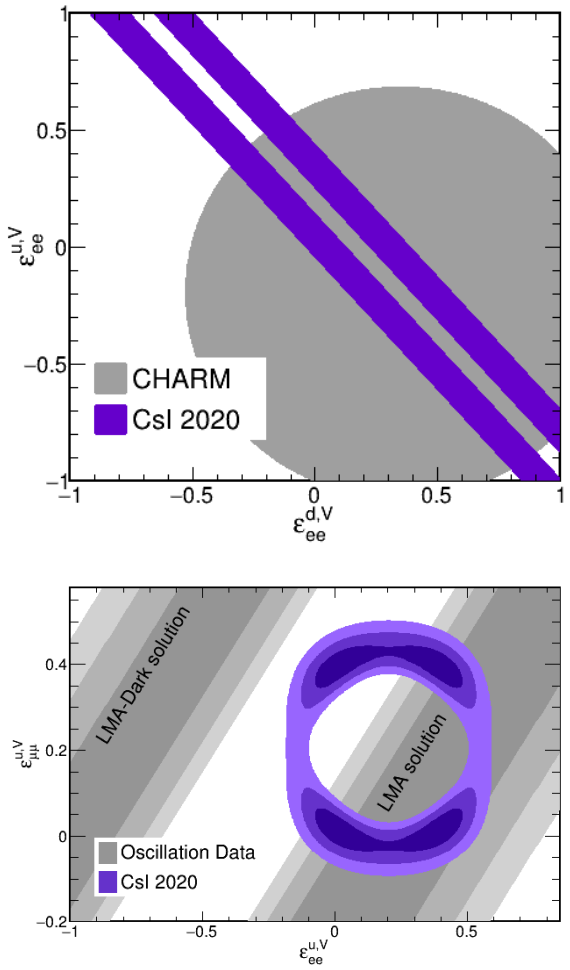

Figure 6. The top plot shows the 90% allowed parameter space with ε_{ee}^{u} and ε_{ee}^{d} to float while fixing others at 0, while the bottom shows $1/2/3\sigma$ contours allowing ε_{ee}^{u} and $\varepsilon_{\mu\mu}^{u}$ to float fixing others to 0. The bottom also shows parameter space that is compatible with a degeneracy in solar neutrino oscillation data that would flip the inferred neutrino mass ordering.

section $\langle\sigma\rangle_{\Phi} = (165^{+30}_{-25}) \times 10^{-40}$ cm^2, consistent with the standard-model prediction to within 1 σ. The weak mixing angle was measured at low-Q^2 using this cross section result. We also introduced measurements of the flavored CEvNS cross section, which are shown to produce improved CEvNS constraints on neutrino-quark NSI scenarios. Though the CsI[Na] detector has been decommissioned, a planned in-situ calibration of the neutrino flux using a heavy-water Cherenkov detector [50] will further improve precision of the CEvNS measurements. COHERENT is currently engaged in future measurements of CEvNS on Ar, Ge, and NaI, while additional targets are possible for the future.

6. ACKNOWLEDGMENTS

The COHERENT collaboration acknowledges the Kavli Institute at the University of Chicago for CsI[Na] detector contributions. The COHERENT collaboration acknowledges the generous resources provided by the ORNL Spallation Neutron Source, a DOE Office of Science User Facility, and thanks Fermilab for the continuing loan of the CENNS-10 detector. We also acknowledge support from the Alfred P. Sloan Foundation, the Consortium for Nonproliferation Enabling Capabilities, the National Science Foundation, the Russian Foundation for Basic Research (proj.# 17-02-01077 A), and the U.S. Department of Energy, Office of Science. Laboratory Directed Research and Development funds from ORNL and Lawrence Livermore National Laboratory also supported this project. This research used the Oak Ridge Leadership Computing Facility, which is a DOE Office of Science User Facility. The work was supported by the Ministry of Science and Higher Education of the Russian Federation, Project Fundamental properties of elementary particles and cosmology No. 0723-2020-0041

[1] D. Z. Freedman, Phys. Rev. D **9**, 1389 (1974).
[2] V. Kopeliovich and L. Frankfurt, JETP Lett. **19**, 145 (1974).
[3] C. L. Cowan, F. Reines, F. B. Harrison, H. W. Kruse, and A. D. McGuire, **124**, 103 (1956).
[4] M. Cadeddu and F. Dordei, Phys. Rev. D **99**, 033010 (2019), arXiv:1808.10202 [hep-ph].
[5] D. Akimov *et al.* (COHERENT), Science **357**, 1123 (2017), arXiv:1708.01294 [nucl-ex].
[6] D. Akimov *et al.* (COHERENT), Phys. Rev. Lett. **126**, 012002 (2021), arXiv:2003.10630 [nucl-ex].
[7] T. E. Mason, T. A. Gabriel, R. K. Crawford, K. W. Herwig, F. Klose, and J. F. Ankner, eConf **C000821**, FR203 (2000), arXiv:physics/0007068.
[8] R. L. Kustom, eConf **C000821**, TU101 (2000), arXiv:physics/0008212.
[9] K. Scholberg, Phys. Rev. D **73**, 033005 (2006), arXiv:hep-ex/0511042.
[10] H. Davoudiasl, H.-S. Lee, and W. J. Marciano, Phys. Rev. D **89**, 095006 (2014), arXiv:1402.3620 [hep-ph].
[11] J. Liao and D. Marfatia, Phys. Lett. B **775**, 54 (2017), arXiv:1708.04255 [hep-ph].
[12] O. Miranda, D. Papoulias, G. Sanchez Garcia, O. Sanders, M. Tórtola, and J. Valle, JHEP **05**, 130 (2020), arXiv:2003.12050 [hep-ph].
[13] B. Abi *et al.* (Muon g-2), Phys. Rev. Lett. **126**, 141801 (2021), arXiv:2104.03281 [hep-ex].

[14] J. Barranco, O. Miranda, and T. Rashba, JHEP **12**, 021 (2005), arXiv:hep-ph/0508299.
[15] P. Coloma, I. Esteban, M. Gonzalez-Garcia, and M. Maltoni, JHEP **02**, 023 (2020), arXiv:1911.09109 [hep-ph].
[16] P. B. Denton, J. Gehrlein, and R. Pestes, (2020), arXiv:2008.01110 [hep-ph].
[17] B. Dutta, S. Liao, S. Sinha, and L. E. Strigari, Phys. Rev. Lett. **123**, 061801 (2019), arXiv:1903.10666 [hep-ph].
[18] D. Akimov *et al.* (COHERENT), Phys. Rev. D **102**, 052007 (2020), arXiv:1911.06422 [hep-ex].
[19] J. Billard, L. Strigari, and E. Figueroa-Feliciano, Phys. Rev. D **89**, 023524 (2014), arXiv:1307.5458 [hep-ph].
[20] C. A. J. O'Hare, Phys. Rev. D **94**, 063527 (2016), arXiv:1604.03858 [astro-ph.CO].
[21] C. Bœhm, D. Cerdeño, P. Machado, A. Olivares-Del Campo, E. Perdomo, and E. Reid, JCAP **01**, 043 (2019), arXiv:1809.06385 [hep-ph].
[22] J. R. Wilson, Phys. Rev. Lett. **32**, 849 (1974).
[23] D. N. Schramm and W. D. Arnett, Phys. Rev. Lett. **34**, 113 (1975).
[24] D. Z. Freedman, D. N. Schramm, and D. L. Tubbs, Annual Review of Nuclear Science **27**, 167 (1977), https://doi.org/10.1146/annurev.ns.27.120177.001123.
[25] K. Balasi, K. Langanke, and G. Martínez-Pinedo, Prog. Part. Nucl. Phys. **85**, 33 (2015), arXiv:1503.08095 [nucl-th].
[26] C. J. Horowitz, K. J. Coakley, and D. N. McKinsey, Phys. Rev. D **68**, 023005 (2003), arXiv:astro-ph/0302071.
[27] R. F. Lang, C. McCabe, S. Reichard, M. Selvi, and I. Tamborra, Phys. Rev. D **94**, 103009 (2016), arXiv:1606.09243 [astro-ph.HE].
[28] B. Abi *et al.* (DUNE), Eur. Phys. J. C **80**, 978 (2020), arXiv:2006.16043 [hep-ex].
[29] K. Abe *et al.* (Super-Kamiokande), Astropart. Phys. **81**, 39 (2016), arXiv:1601.04778 [astro-ph.HE].
[30] P. S. Amanik and G. C. McLaughlin, Journal of Physics G: Nuclear and Particle Physics **36**, 015105 (2008).
[31] J. Collar, N. Fields, M. Hai, T. Hossbach, J. Orrell, C. Overman, G. Perumpilly, and B. Scholz, Nucl. Instrum. Meth. A **773**, 56 (2015), arXiv:1407.7524 [physics.ins-det].
[32] N. E. Fields, *CosI: Development of a low threshold detector for the observation of coherent elastic neutrino-nucleus scattering*, Ph.D. thesis, The University of Chicago (2014).
[33] S. Agostinelli *et al.* (GEANT4), Nucl. Instrum. Meth. A **506**, 250 (2003).
[34] D. Akimov *et al.*, (2021), arXiv:2109.11049 [hep-ex].
[35] B. J. Scholz, *First Observation of Coherent Elastic Neutrino-Nucleus Scattering*, Ph.D. thesis, Chicago U. (2017), arXiv:1904.01155 [nucl-ex].
[36] J. Collar, A. Kavner, and C. Lewis, Phys. Rev. D **100**, 033003 (2019), arXiv:1907.04828 [nucl-ex].
[37] Eljen Technology, 1300 W. Broadway St., Sweetwater, TX 79556.
[38] S. A. Pozzi, E. Padovani, and M. Marseguerra, Nuclear Instruments and Methods in Physics Research Section A: Accelerators, Spectrometers, Detectors and Associated Equipment **513**, 550 (2003).
[39] S. Gardiner, *Nuclear Effects in Neutrino Detection*, Ph.D. thesis, University of California, Davis (2018).
[40] S. Gardiner, "MARLEY (Model of Argon Reaction Low Energy Yields)," (2020).
[41] V. A. Bednyakov and D. V. Naumov, Phys. Rev. D **98**, 053004 (2018), arXiv:1806.08768 [hep-ph].
[42] S. S. Wilks, Ann. Math. Statist. **9**, 60 (1938).
[43] D. Androic *et al.* (Q_{weak} Collaboration), Phys. Rev. Lett. **111**, 141803 (2013).
[44] P. Zyla *et al.* (Particle Data Group), PTEP **2020**, 083C01 (2020).
[45] C. S. Wood, S. C. Bennett, D. Cho, B. P. Masterson, J. L. Roberts, C. E. Tanner, and C. E. Wieman, **275**, 1759 (1997).
[46] V. A. Dzuba, J. C. Berengut, V. V. Flambaum, and B. Roberts, Phys. Rev. Lett. **109**, 203003 (2012).
[47] J. Dorenbosch *et al.*, Physics Letters B **180**, 303 (1986).
[48] E. Aprile *et al.* (XENON), (2020), arXiv:2012.02846 [hep-ex].
[49] P. Coloma, M. Gonzalez-Garcia, M. Maltoni, and T. Schwetz, Phys. Rev. D **96**, 115007 (2017), arXiv:1708.02899 [hep-ph].
[50] D. Akimov *et al.*, Journal of Instrumentation **16**, P08048 (2021).

Appendix A: Release of analysis data

We provide selected, unbinned data events relevant for this result. We also provide signal parameters, neutron background distributions, and details of systematic uncertainty to allow for future study of this analysis sample. All events selected with PE < 250 and $0 \leq t_{\rm rec} < 6$ μs are included. Events with energy $60 \leq$ PE < 250 are not used for measuring the CEvNS cross section but used for a search for light dark matter produced at the SNS.

1. Data

Selected events in both the coincidence (C) and anticoincidence (AC) region for beam-on running are given in

- dataBeamOnAC.txt
- dataBeamOnC.txt.

each with reconstructed energy, $E_{\rm rec}$, and recoil time, $t_{\rm rec}$. A comparison of C and AC data is shown in Fig. 7 with a clearly visible beam excess. These two files contain all data relevant for this measurement. The requisite details to produce accurate predictions for signal and background distributions are below.

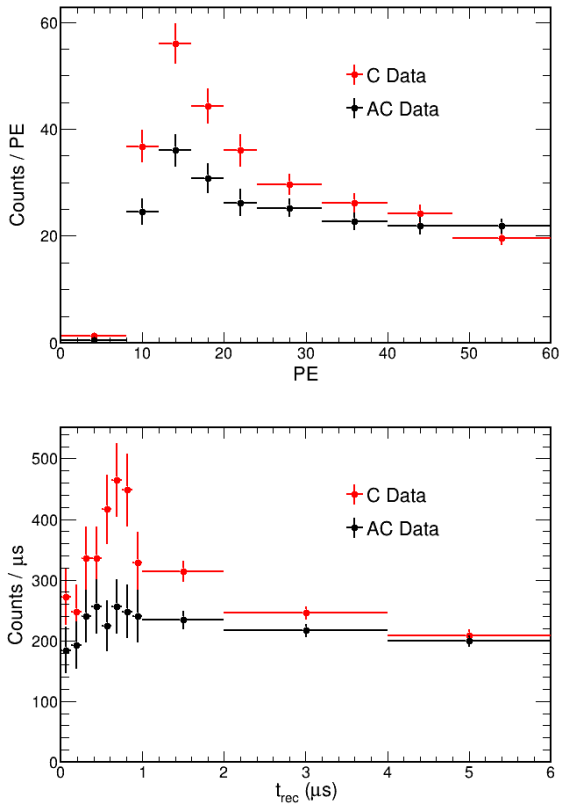

Figure 7. Selected data collected during SNS operations comparing C and AC ROI data.

2. Steady-state background

The beam-uncorrelated, steady-state background can be estimated from the AC data. For selected events, there is no correlation between $E_{\rm rec}$ and $t_{\rm rec}$, and thus the $E_{\rm rec}$ distribution can be determined using all selected events. The time distribution is exponential with a decay constant

- $k = -(0.0494 \pm 0.0061)/\mu$s

determined by fitting the timing distribution of AC events.

3. Neutron backgrounds

We include both prompt beam-related neutron (BRN) and neutrino-induced neutron (NIN) events. The reconstructed energy and time are uncorrelated, and so we include the one-dimensional projections in PE and $t_{\rm rec}$. For each, we provide the timing distribution in 0.01 μs bins normalized to the beam exposure, 13.99 GWhr. We include the prediction for times $-0.25 \leq t_{\rm rec} < 6.25$ μs, to accommodate uncertainty in beam timing. Due to this uncertainty in timing, the time dependent efficiency, ε_T, is not applied. This can be included as

$$\varepsilon_T(t_{rec}) = \begin{cases} 1 & t_{rec} < a \\ e^{-b(t_{rec}-a)} & t_{rec} \geq a \end{cases} \quad \text{(A1)}$$

with

- a = 0.52 μs
- b = 0.0494 /μs.

The smeared PE probability distribution with the energy dependent efficiency, $\varepsilon_{\rm PE}$, applied is included with 1 PE binning. All energy shape uncertainties in both backgrounds have a negligible impact and are not included. These distributions are included as text files:

- brnPE.txt
- brnTrec.txt
- ninPE.txt
- ninTrec.txt.

4. Signal Prediction Parameters

We analyze beam triggers from 13.99 GWhr of accumulated exposure. The neutrino flux through the detector and rate of CEvNS scatters can be calculated with the parameters:

- POT: 3.198 $\times 10^{23}$
- ν yield: $0.0848 \pm 10\%$ ν/flavor/p
- Detector baseline 19.3 m
- Detector mass: 14.6 kg.

The 2D distribution of the neutrino flux at the SNS is given in

- snsFlux2D.root

with a ROOT histogram for each flavor in the flux.

To accurately predict the event totals in the detector as a function of $E_{\rm rec}$ and $t_{\rm rec}$, quenching, energy smearing, and detection efficiency must be applied.

Quenching is applied by evaluating the scintillation response curve, empirically parameterized as

$$E_{ee} = f(E_{nr}) = aE_{nr} + bE_{nr}^2 + cE_{nr}^3 + dE_{nr}^4. \quad \text{(A2)}$$

The best-fit coefficients are provided in

- scintRespCoefficients.txt.

The file also includes coefficients for each of the two quenching uncertainties included, evaluated at $\pm 1\sigma$ excursions. The light yield for quenched recoils is given by

- Light yield: 13.35 photons/keVee

whose uncertainty has a negligible impact.

Energy smearing is applied according to a gamma distribution

$$\frac{[a(1+b)]^{1+b}}{\Gamma(1+b)} x^b e^{-a(1+b)x} \tag{A3}$$

with parameters

$$a = 1/\mathrm{PE} \tag{A4}$$

$$b = 0.716 \times \mathrm{PE}. \tag{A5}$$

Our analysis of the CEvNS cross section made sure to not include energy bins much narrower than the energy resolution. It is essential for any study using finer bins or an unbinned fit to include smearing effects.

Finally, efficiency must also be applied.

$$\varepsilon(\mathrm{PE}, t_{\mathrm{rec}}) = \varepsilon_E(\mathrm{PE}) \times \varepsilon_T(t_{\mathrm{rec}}) \tag{A6}$$

which contains uncorrelated factors from the measured E_{rec} and t_{rec}. We parameterize ε_E as

$$\varepsilon_E(x) = \frac{a}{1 + e^{-b(x-c)}} + d \tag{A7}$$

where x is the observed recoil energy in PE and the function is restricted to evaluate at ≥ 0. The relevant coefficients in the best fit scenario and are included in

- effCoefficients.txt

along with coefficients evaluated at $\pm 1\sigma$ excursions for the uncertainty in the CEvNS efficiency. The time dependence is given in Eqn. A1.